

# Torsion of a cylinder of partially molten rock with a spherical inclusion: theory and simulation

Laura Alisic\*   Sander Rhebergen†   John F. Rudge‡   Richard F. Katz§  
Garth N. Wells¶

## Abstract

The processes that are involved in migration and extraction of melt from the mantle are not yet fully understood. Gaining a better understanding of material properties of partially molten rock could help shed light on the behavior of melt on larger scales in the mantle. In this study, we simulate three-dimensional torsional deformation of a partially molten rock that contains a rigid, spherical inclusion. We compare the computed porosity patterns to those found in recent laboratory experiments. The laboratory experiments show emergence of melt-rich bands throughout the rock sample, and pressure shadows around the inclusion. The numerical model displays similar melt-rich bands only for a small bulk-to-shear-viscosity ratio (five or less). The results are consistent with earlier two-dimensional numerical simulations; however, we show that it is easier to form melt-rich bands in three dimensions compared to two. The addition of strain-rate dependence of the viscosity causes a distinct change in the shape of pressure shadows around the inclusion. This change in shape presents an opportunity for experimentalists to identify the strain-rate dependence and therefore the dominant deformation mechanism in torsion experiments with inclusions.

## 1 Introduction

The transport of melt in the mantle plays an important role in the dynamics and chemical evolution of both the mantle and the crust. Although the equations that describe the conservation of mass, momentum, and energy of partially molten rock are well established (*McKenzie*, 1984; *Bercovici and Ricard*, 2003), the appropriate constitutive relations remain uncertain. This means that the dynamics of melt segregation and transport present significant unanswered questions.

One means of addressing questions on the dynamics of melt segregation and transport is by comparison of simulations with laboratory experiments on partially molten rocks subjected to forced deformation. A recent experimental study with significant potential in this regard is reported by *Qi et al.* (2013). Following on the torsional deformation experiments of *King et al.* (2010), *Qi et al.* (2013) modified the basic experiment by including rigid, spherical beads within the partially molten rock that is undergoing deformation. They find that pressure shadows around the bead are expressed as variations in melt fraction there. Furthermore, they find that melt-rich bands, also observed in experiments without beads (e.g. *Holtzman et al.*, 2003), emerge and tend to connect with the large-porosity lobes of the pressure shadow. Previous analysis of pressure shadows (*McKenzie and Holness*, 2000; *Rudge*, 2014) and their interaction with banding instabilities (*Alisic et al.*, 2014) suggests that the observed relationship between these two modes of compaction could constrain the bulk viscosity of the two-phase system.

---

\*Department of Earth Sciences, University of Cambridge, Cambridge, United Kingdom (now at Jet Propulsion Laboratory, California Institute of Technology, USA).

†Department of Applied Mathematics, University of Waterloo, Canada.

‡Department of Earth Sciences, University of Cambridge, United Kingdom.

§Department of Earth Sciences, University of Oxford, United Kingdom.

¶Department of Engineering, University of Cambridge, Cambridge, United Kingdom.

In working towards a better understanding of compaction in a two-phase system, we pose the following questions about the viscosity of the two-phase system that remain unresolved. What is the ratio of the bulk viscosity to the shear viscosity at small reference porosity (*Simpson et al.*, 2010)? How do the bulk and shear viscosities vary with porosity (e.g. *Kelemen et al.*, 1997; *Mei et al.*, 2002; *Takei and Holtzman*, 2009)? Is the rheology non-Newtonian and, if so, does this help to explain the patterns observed in experiments? And, more broadly, is a solely viscous rheology sufficient to capture the dynamics? These are long-term questions that we address. However, we find that on the basis of the comparison between experiments and theory considered here, we cannot answer these questions definitively, and we present a discussion of this shortcoming.

In an earlier paper, we developed two-dimensional models of two-phase flow around a cylindrical inclusion to study the same experimental system (*Alisic et al.*, 2014). Here we build on those results by expanding the numerical simulations to three dimensions. This allows us to capture the three-dimensional scaling of compaction around a sphere, which differs from the two-dimensional scaling around a cylinder (*Rudge*, 2014). Moreover, the simulations presented here provide a more realistic comparison to the results of laboratory experiments (*Qi et al.*, 2013). These new simulations with  $\sim 7 \times 10^6$  degrees of freedom would be impossible without an advanced, new preconditioning method for the equations of magma dynamics that has been recently developed (*Rhebergen et al.*, 2015).

We begin this manuscript with a description of the equations governing deformation and compaction of partially molten rock, after which we summarize the domain geometry, boundary conditions, and discretization used in the numerical simulations. Analytical solutions for certain limiting cases are provided in Appendix B; we use these to benchmark the simulation code. The first set of results in Section 3.1 pertains to simulations with a uniform initial porosity that allow us to focus on compaction around a spherical inclusion in three dimensions, with Newtonian and non-Newtonian rheology. The simulations in Section 3.2 focus on problems with a random initial porosity field, where we investigate the interaction between pressure shadows around the inclusion and melt-rich bands developing throughout the domain. The results are followed by a discussion in Section 4, after which conclusions are drawn.

## 2 The model

### 2.1 Governing equations

The compaction of partially molten rock and the transport of melt can be described by governing equations for two-phase flow, formulated here following *McKenzie* (1984). In dimensionless form (see Appendix A for the nondimensionalization):

$$\frac{\partial \phi}{\partial t} - \nabla \cdot (1 - \phi) \mathbf{u}_s = 0, \quad (1)$$

$$-\nabla \cdot \mathbf{u}_s + \nabla \cdot \left( \frac{D^2}{R + \frac{4}{3}} K_\phi \nabla p_f \right) = 0, \quad (2)$$

$$-\nabla \cdot \mathbf{u}_s - (R\zeta)^{-1} p_c = 0, \quad (3)$$

$$-\nabla \cdot \bar{\boldsymbol{\tau}} + \nabla p_f + \nabla p_c = \mathbf{0}, \quad (4)$$

where  $t$  denotes time,  $\phi$  is porosity,  $\mathbf{u}_s$  is the solid (matrix) velocity,  $p_f$  and  $p_c$  are the magma and compaction pressure, respectively, and  $\bar{\boldsymbol{\tau}}$  is the deviatoric stress in the solid. Constitutive properties, discussed further below, appear as  $K_\phi$  for the permeability and  $\zeta$  for the bulk viscosity. The bulk-to-shear-viscosity ratio in the reference state is defined as  $R = \zeta_{\text{ref}}/\eta_{\text{ref}}$ , where  $\zeta_{\text{ref}}$  is a reference bulk viscosity and  $\eta_{\text{ref}}$  is a reference shear viscosity for the two-phase mixture. Finally,  $D = \delta/H$  where  $\delta$  is the compaction length and  $H$  is the height of the domain. The

compaction length is given by (McKenzie, 1984):

$$\delta = \sqrt{\frac{\left(R + \frac{4}{3}\right) \eta_{\text{ref}} K_{\text{ref}}}{\mu_f}}, \quad (5)$$

where  $K_{\text{ref}}$  is the permeability in the reference state, and  $\mu_f$  is the magma viscosity. In this study we assume a compaction length that is much larger than the domain size ( $D = 100$ ). The deviatoric stress tensor  $\bar{\tau}$  is

$$\bar{\tau} = \eta \underbrace{\left( \nabla \mathbf{u}_s + (\nabla \mathbf{u}_s)^T - \frac{2}{3} (\nabla \cdot \mathbf{u}_s) \mathbf{I} \right)}_{2\dot{\epsilon}}, \quad (6)$$

where  $\eta$  is the shear viscosity and  $\dot{\epsilon}$  is the deviatoric strain-rate tensor.

The above model assumes that no melting or solidification takes place, buoyancy forces are negligible, and that the fluid and solid phases have densities that are constant (but different from each other); these assumptions are appropriate for the motivating laboratory experiments (e.g. Holtzman *et al.*, 2003), though a model for the Earth’s mantle clearly must be more general. The unknown fields in the model are  $\phi$ ,  $\mathbf{u}_s$ ,  $p_f$ , and  $p_c$ , which must satisfy equations (1)–(4), subject to the boundary conditions described below.

## 2.2 Rheology and permeability

Closure conditions for the governing equations are prescribed as

$$K_\phi = \left( \frac{\phi}{\phi_0} \right)^n, \quad \eta = (2\dot{\epsilon})^{-q} e^{-\alpha(\phi-\phi_0)}, \quad \zeta = \underbrace{(2\dot{\epsilon})^{-q} e^{-\alpha(\phi-\phi_0)}}_{\eta} \left( \frac{\phi}{\phi_0} \right)^{-m}, \quad (7)$$

where  $n$  and  $m$  depend on the melt geometry considered. We take  $n = 2$  and  $m = 1$ , assuming a tubular melt geometry. In these definitions,  $\phi_0$  is the reference porosity,  $\alpha$  is a constant representing the sensitivity of matrix shear viscosity to porosity,  $\dot{\epsilon}$  is the second invariant of the deviatoric strain-rate tensor,

$$\dot{\epsilon} = \left( \frac{1}{2} \dot{\epsilon} : \dot{\epsilon} \right)^{1/2}, \quad (8)$$

and  $q$  is related to the power-law exponent  $\mathbf{n}$  by

$$q = 1 - \frac{1}{\mathbf{n}}. \quad (9)$$

A power-law exponent  $\mathbf{n} = 1$  gives the limit of Newtonian rheology.

In this study we focus on the effects of the porosity sensitivity  $\alpha$ , the reference bulk-to-shear-viscosity ratio  $R$ , and the power-law exponent  $\mathbf{n}$  on compaction patterns around and away from an inclusion. Laboratory experiments indicate that  $\alpha$  is around 26 for a Newtonian rheology (diffusion creep) and around  $31/\mathbf{n}$  for dislocation creep (Kelemen *et al.*, 1997; Mei *et al.*, 2002). Several previous modelling studies have used a value  $\alpha = 28$  (e.g. Alisic *et al.* (2014); Katz *et al.* (2006)). The bulk-to-shear-viscosity ratio, however, is poorly constrained. Theoretical and experimental studies place  $R$  between order one, independent of the reference porosity (Takei and Holtzman, 2009), and  $\sim 20$  for a reference porosity  $\phi_0 = 0.05$  on the basis of the expected relation  $R \propto \phi^{-1}$  (Bercovici and Ricard, 2003; Simpson *et al.*, 2010). In the simulations presented here, we vary  $\alpha$  between zero and 50, and  $R$  between  $5/3$  and 20. In simulations where we study the effect of strain-rate dependence of the shear and bulk viscosities, the power-law exponent  $\mathbf{n}$  has values between 1 and 6. The deformation mechanism of diffusion creep corresponds to  $\mathbf{n} = 1$ , resulting in Newtonian viscosities. A larger exponent of around 3 to 4 is relevant for dislocation creep. Katz *et al.* (2006) showed that increasing the power-law exponent is one possible mechanism for reproducing the shallow angle of melt-rich bands as observed in laboratory experiments. We therefore include simulations with  $\mathbf{n}$  up to six.

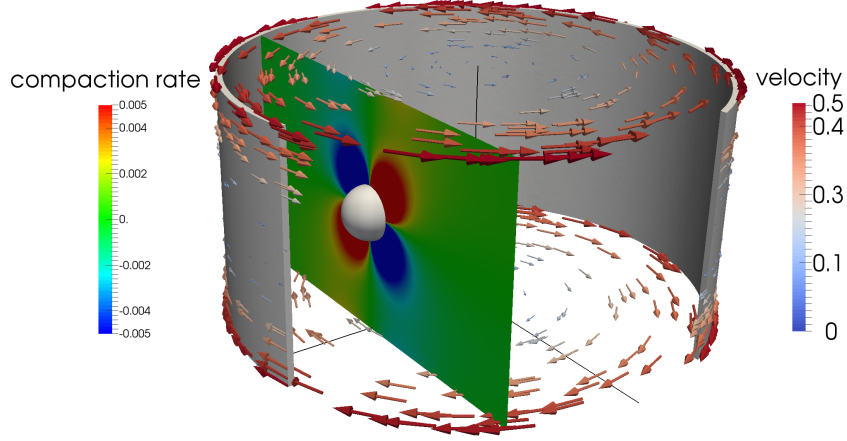


Figure 1: The geometry of the model domain: a cylinder of height  $H = 1$  and radius one (only a thin cut-out is shown in light gray), with a rigid spherical inclusion of radius 0.1. On a two-dimensional slice through the cylinder and inclusion at  $x = \frac{1}{2}$ , the instantaneous compaction rate  $(\nabla \cdot \mathbf{u}_s)$  is plotted for a simulation with bulk-to-shear-viscosity ratio  $R = 20$ , and power-law exponent  $\mathbf{n} = 1$  at time  $t = 0$ . The arrows at the top, bottom and side of the cylinder indicate the prescribed solid velocity on the cylinder boundaries.

### 2.3 Domain of interest and boundary and initial conditions

We compute solutions to equations (1)–(4) in a cylindrical domain  $\Omega \subset \mathbb{R}^3$  of height  $H = 1$  and radius 1, where  $x^2 + y^2 \leq 1$  and  $0 \leq z \leq 1$ . A rigid spherical inclusion is centered at  $\mathbf{r}_0 = (1/2, 0, 1/2)$  and has a radius of 0.1, as shown in Figure 1. The inclusion is modeled as a spherical hole in the domain that cannot deform. The boundary conditions are defined on the boundary  $\partial\Omega$  as:

$$K_\phi \nabla p_f \cdot \mathbf{n} = 0 \text{ on } \partial\Omega, \quad (10)$$

$$\mathbf{u}_s = \mathbf{w} \text{ on } \partial\Omega, \quad (11)$$

where the boundaries are taken to be impermeable (equation (10)), and  $\mathbf{w}$  is a prescribed solid velocity. The cylinder is placed under torsion. This torsion is enforced by Dirichlet boundary conditions of the form (11) on the top and bottom ( $z = 0$  and  $z = 1$ ), and side boundaries of the cylinder ( $x^2 + y^2 = 1$ ), such that on the outside of the cylinder  $\mathbf{w} = \mathbf{u}_{\text{cyl}}$ :

$$\mathbf{u}_{\text{cyl}} = \left( -y \left( z - \frac{1}{2} \right), x \left( z - \frac{1}{2} \right), 0 \right). \quad (12)$$

Formally, the boundary conditions on the rigid inclusion are conditions of no net force and no net torque (see *Alisic et al. (2014, Appendix B)*). Here, to simplify the construction of the numerical model, we instead apply a Dirichlet boundary condition of the form (11) that approximates the zero net force and torque conditions. In a uniform medium, a rigid sphere placed at the mid-plane of a torsion field should not translate, but should rotate with an angular velocity equal to half the vorticity of the imposed torsion field (see Section B.1). Thus we use a Dirichlet condition on the boundary of the inclusion with  $\mathbf{w} = \mathbf{u}_{\text{sphere}}$ ,

$$\mathbf{u}_{\text{sphere}} = \boldsymbol{\Omega} \times (\mathbf{r} - \mathbf{r}_0), \quad (13)$$

where  $\mathbf{r} = (x, y, z)$  is the position vector, and  $\mathbf{r}_0$  is the center of the sphere. The angular velocity  $\boldsymbol{\Omega}$  is given by

$$\boldsymbol{\Omega} = \frac{1}{2} \nabla \times \mathbf{u}_{\text{cyl}}|_{\mathbf{r}=\mathbf{r}_0} = \left( -\frac{1}{4}, 0, 0 \right). \quad (14)$$



In our Cartesian coordinate system and for the position of the inclusion, (13) can thus be written

$$\mathbf{u}_{\text{sphere}} = \left( 0, \frac{1}{4} \left( z - \frac{1}{2} \right), -\frac{1}{4}y \right). \quad (15)$$

The placement of the inclusion at  $x = 1/2$  results in a local strain at the center of the inclusion equal to half the total, outer-radius model strain, which scales to half the model time in a simulation.

We choose either a constant initial porosity field with  $\phi_0 = 0.05$ , or a random initial porosity with uniformly distributed values in the range  $\phi_0 \pm 5 \times 10^{-3}$ . For the simulations with a randomly perturbed initial porosity field, we produced one initial field and reused this for all simulations. This initial field is created by first generating a random field on a uniform mesh that has a slightly larger grid size than the largest elements in the cylinder mesh; then this is interpolated onto the cylindrical mesh containing the spherical hole and variable grid size. This approach ensures that the random perturbations are sufficiently resolved by the mesh used in simulations and that the length scale of the perturbations does not vary with element size.

Throughout this paper, we present simulation results on a two-dimensional slice through the inclusion at  $x = 1/2$ , as shown in Figure 1. In this figure, the instantaneous compaction rate at time  $t = 0$  for a simulation with bulk-to-shear-viscosity ratio  $R = 20$  is shown on the slice. The initial compaction rate is independent of the porosity exponent  $\alpha$  for uniform porosity initial conditions. Pressure gradients caused by flow past the spherical inclusion induce two compacting lobes and two dilating lobes around the inclusion. This behavior was described in detail by *McKenzie and Holness* (2000); *Alisic et al.* (2014); *Rudge* (2014) and is discussed further in Section B.1.

## 2.4 Discretization

The problem described in Section 2.3 is solved by a finite element method on a mesh of tetrahedral cells consisting of approximately 50 cells in the vertical dimension. The mesh is refined around the inclusion. The smallest cell size is  $\sim 3 \times 10^{-3}$  near the inclusion, and the largest cell size is  $\sim 7 \times 10^{-2}$  away from it.

There are two main time stepping approaches to solving the two-phase flow equations (1)–(4), namely, as a fully coupled system (*Katz et al.*, 2007) or by decoupling the porosity evolution equation (1) from the compaction equations (2)–(4) (*Katz and Takei*, 2013). We follow the second approach. At each time step, equations (2)–(4) are solved to find the solid velocity, fluid pressure and compaction pressure, given the porosity and viscosities from the previous iteration. The porosity is then updated by solving (1). To ensure a good approximation of the coupling, we iterate this process. Furthermore, if a non-Newtonian rheology is used, within each iteration a new strain rate is computed from the solid velocity and the viscosities are updated accordingly.

The compaction system (2)–(4) is discretized with a continuous Galerkin finite element method using Taylor–Hood type elements (piecewise quadratic polynomial approximation for the solid velocity and piecewise linear polynomial approximation for the fluid and compaction pressures, see *Rhebergen et al.* (2014)). The system of linear equations resulting from this discretization is solved using Bi-CGSTAB in combination with the block-preconditioners developed in *Rhebergen et al.* (2015).

The porosity evolution equation (1) is discretized in space by a discontinuous Galerkin finite element method using a linear polynomial approximation. A Crank–Nicolson time stepping scheme is used to discretize in time (but using only the most recently computed velocity). To stabilize the simulation, a porosity-gradient-dependent artificial diffusion is added to the porosity evolution equation (1) of the form  $\epsilon \nabla \cdot (|\nabla \phi|^3 \nabla \phi)$ , with  $\epsilon = 0.1$ . To solve the resulting discrete system we use restarted GMRES preconditioned by algebraic multigrid. Simulations are terminated when the porosity becomes smaller than zero or larger than unity.

Instead of solving (2)–(4), it is possible to eliminate the compaction pressure by substituting (3) into (4). The reduced system has fewer unknowns, but solving it is numerically less robust and less efficient than solving the expanded system (2)–(4). We refer to *Rhebergen et al.* (2015) for more details.

Our simulation code is developed within the finite element software framework FEniCS/DOLFIN (*Logg et al.*, 2012; *Logg and Wells*, 2010), in conjunction with the PETSc linear algebra and solver library (*Balay et al.*, 2015a,b).

### 3 Results

We group our results into two categories. In the first, the porosity is initially uniform. This means that the initial growth rate of the melt-banding instability is zero, and hence that changes in porosity are initially due solely to the presence of the inclusion. We consider the sensitivity of the compaction pattern to problem parameters, including the stress-dependence of the viscosity. The second category uses an initial condition with a random porosity perturbation. Melt-rich bands can potentially develop from the outset in this class of simulations. We explore in detail how and when such melt-rich bands develop, and how they interact with pressure shadows around the inclusion.

#### 3.1 Uniform initial porosity

**Newtonian viscosity** We investigate the effect of the porosity exponent  $\alpha$  and bulk-to-shear-viscosity ratio  $R$  on the porosity evolution in time-dependent simulations with a uniform initial porosity of  $\phi_0 = 0.05$  and Newtonian viscosity. When  $\alpha = 0$  and  $\mathbf{n} = 1$ , the shear viscosity is constant and uniform. In this case, the pressure shadows around the inclusion that are identified by perturbations in the porosity field rotate and advect with the matrix, with the top moving to the right and the bottom to the left, as shown in Figure 2a and c (note that all cross-sections presented in this paper are oriented to have the same direction of shear). In contrast, in a simulation with  $\alpha = 28$  and  $\mathbf{n} = 1$ , shown in Figure 2b and d, the pressure shadows change shape in the opposite direction over time, following the orientation of expected bands in an inhomogeneous model (e.g. *Spiegelman*, 2003).

To study the behavior of pressure shadows in more detail, we compute integrals of porosity on the two-dimensional slice through the inclusion. Integration is from the local radius of the edge of the inclusion  $r = a$  to one inclusion radius outward at  $r = 2a$ , for a series of azimuths between 0 and  $2\pi$  around the circular cross-section of the inclusion (*Qi et al.*, 2013; *Alisic et al.*, 2014)

$$\frac{1}{a} \int_a^{2a} \phi \, dr. \quad (16)$$

Such radial integrals of porosity around the inclusion help expose the effect of  $\alpha$  on the time evolution of pressure shadows. For the  $\alpha = 0$  simulation, the peaks become sharper over time, and the troughs become wider (see Figure 2e). The opposite happens for the  $\alpha = 28$  model (see Figure 2f), with widening peaks. These differences are more pronounced for smaller bulk-to-shear-viscosity ratios  $R$ , as seen in Figure 3. These results are consistent with the two-dimensional results presented in *Alisic et al.* (2014).

**Non-Newtonian viscosity** We introduce a non-Newtonian, power-law rheology in time-dependent simulations with uniform initial porosity. In these simulations, the power-law exponent  $\mathbf{n}$  is larger than one. The geometry of pressure shadows around the inclusion is affected by this strain-rate dependence, and ‘spokes’ form on either side of each pressure shadow quadrant in a simulation with  $\alpha = 0$ , as shown in Figure 4a-b. This pattern is similar to the shape of pressure anomalies in non-Newtonian materials under simple shear found by *Tenczer et al.*

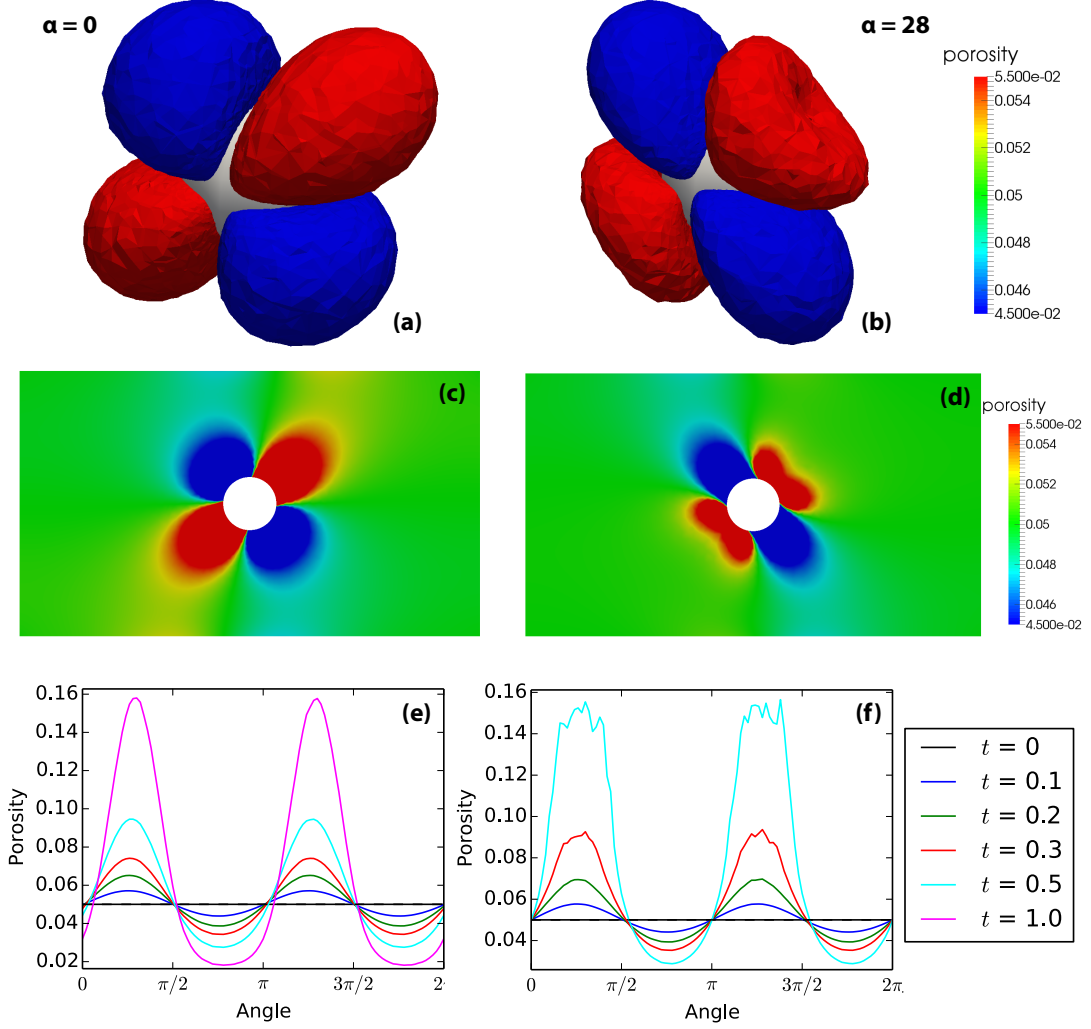


Figure 2: Results for simulations with a uniform initial porosity field and Newtonian shear viscosity ( $n = 1$ ). The local strain at the center of the inclusion corresponds to one half of the reported model time. **(a)** Three-dimensional view of the porosity field for a simulation with porosity exponent  $\alpha = 0$ , bulk-to-shear-viscosity ratio  $R = 5$ , at time  $t = 0.5$  corresponding to a local strain of 0.25 at the center of the inclusion. The pressure shadows around the inclusion are shown as porosity contours of 0.045 in blue and 0.055 in red. **(b)** Three-dimensional view of the porosity field for a simulation with  $\alpha = 28$  and  $R = 5$ , at time  $t = 0.5$ , with porosity contours at 0.045 and 0.055. **(c)** Slice through the porosity field at  $x = \frac{1}{2}$ , for the simulation with  $\alpha = 0$ ,  $R = 5$ , at  $t = 0.5$ . **(d)** Slice through the porosity field, for the simulation with  $\alpha = 28$ ,  $R = 5$ , at  $t = 0.5$ . **(e)** Radial integrals over porosity, for the simulation with  $\alpha = 0$ ,  $R = 5$ , at various times  $t$ . **(f)** Radial integrals over porosity, for the simulation with  $\alpha = 28$ ,  $R = 5$ , at various times  $t$ .

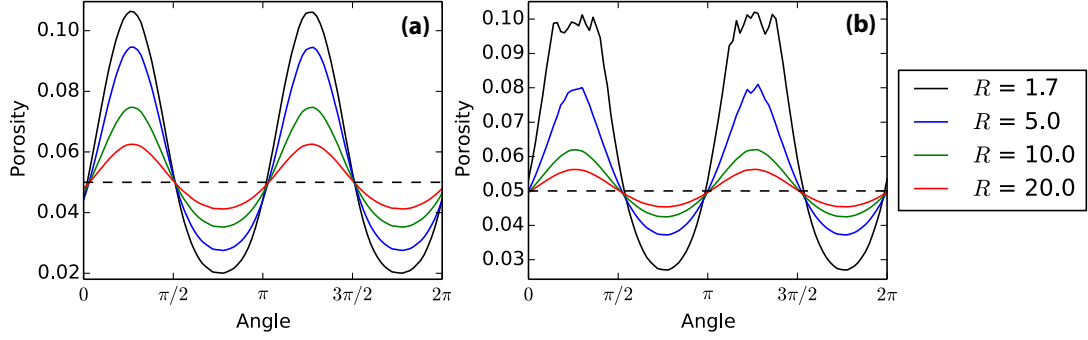


Figure 3: Radial integrals over porosity for simulations with uniform initial porosity field and  $n = 1$ , with various values of bulk-to-shear-viscosity ratio  $R$ . **(a)** Simulations with  $\alpha = 0$  at time  $t = 0.5$ , for various values of  $R$ . **(b)** Simulations with  $\alpha = 28$  at time  $t = 0.25$  or a local strain of 0.125 at the center of the inclusion, for various values of  $R$ .

(2001). The second invariant of the strain-rate, shown in Figure 4c and which controls the viscosity variations, exhibits a complex pattern around the inclusion, without significant temporal variation throughout the simulation time.

An increase in the power-law exponent  $n$  results in more pronounced spokes in the pressure shadows. However, these spokes mostly develop further than one inclusion radius away from the edge of the inclusion, and therefore the spoke shape is not reflected in the radial integrals (see Figure 4d-e). Figure 4e further indicates that there is a decrease in amplitude of the peaks and troughs of the radial integrals for an increase in  $n$ . This implies that the strain-rate dependence of the viscosity does not enhance porosity growth rates.

Increasing the porosity exponent  $\alpha$  up to 28 (not shown here) does not result in a significant change of geometry of the pressure shadows in simulations with a total strain up to 0.2, indicating that the strain-rate dependence of the rheology is dominant over the porosity dependence at low strains. It is to be expected that at larger strains, when porosity anomalies have developed larger amplitudes, the porosity dependence becomes more significant. This could then lead to larger differences in geometry for  $\alpha = 0$  and 28. In contrast to porosity gradients, gradients in the strain-rate are large from the onset of simulations, as illustrated by Figure 4c. The localized distribution of the strain-rate variations around the inclusion presents a significant resolution challenge for the numerical simulations. It has therefore proven difficult to model high strains for large values of  $n$ .

### 3.2 Non-uniform initial porosity

We now present simulations with a Newtonian rheology and initial porosity perturbations with a maximum amplitude of  $\pm 5 \times 10^{-3}$  about a background porosity  $\phi_0$  of 0.05. The initial porosity field, shown in Figure 5a, is the same for all simulations presented in this section.

In a simulation with porosity exponent  $\alpha = 28$  and bulk-to-shear-viscosity ratio  $R = 1.7$ , melt-rich bands develop throughout the cylinder over time at an angle of  $\sim 45^\circ$  with respect to the top and bottom of the domain (Figure 5b). Larger band amplitudes are found towards the outside of the cylinder, as the local strain is proportional to the radius. Melt-rich bands develop both around the inclusion and away from it as shown in cross-sections at  $x = 1/2$  through the inclusion and at  $x = -1/2$  through the opposite side of the cylinder in Figure 6a and c. In contrast, a simulation with the same  $\alpha$  and  $R = 20$  does not display the formation of melt-rich bands, as shown in Figure 6b and d.

The integrals in Figure 6e-f illustrate the difference in behavior between the  $R = 1.7$  and  $R = 20$  simulations: the widening and flattening of the high-porosity peaks is much more visible

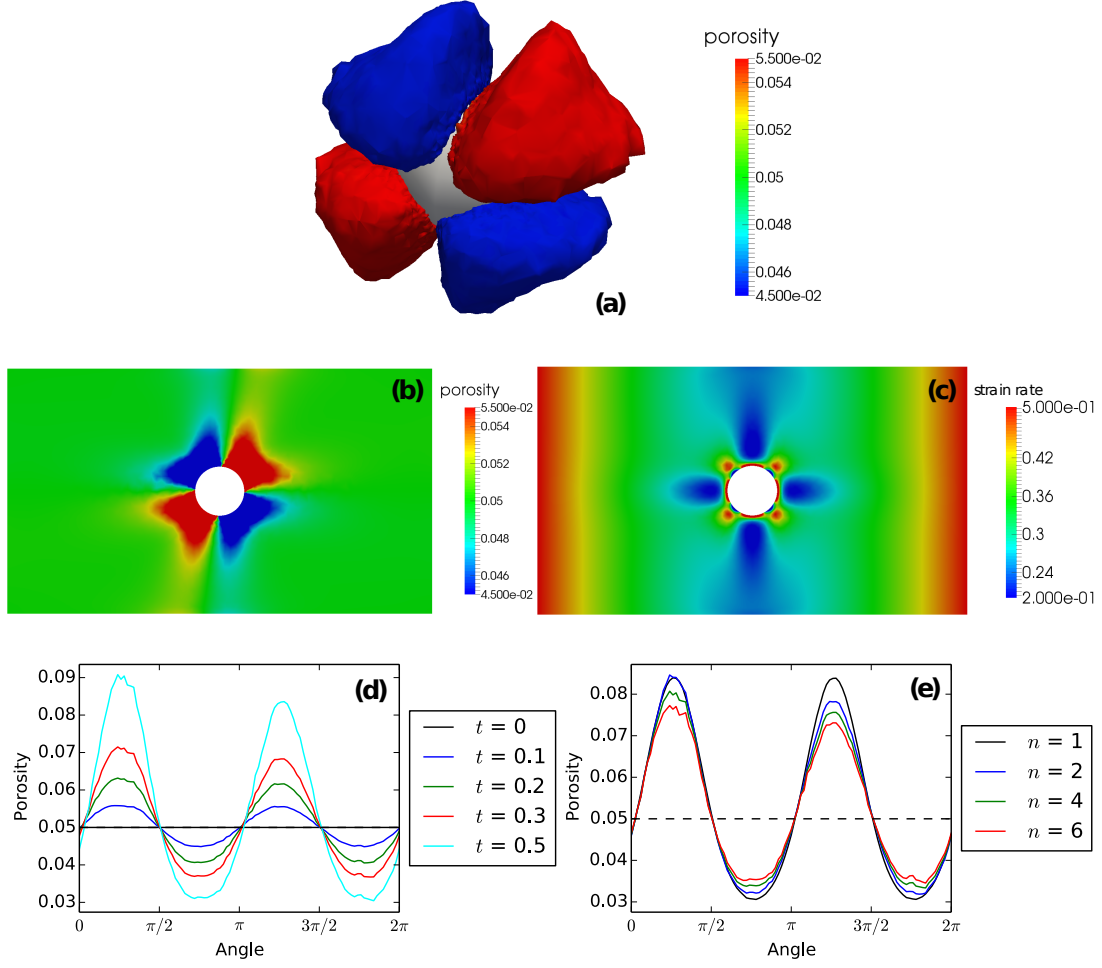


Figure 4: Results for simulations with a uniform initial porosity field and a non-Newtonian shear viscosity. The local strain at the center of the inclusion corresponds to one half of the reported model time. (a) Three-dimensional view of the porosity field for a simulation with porosity exponent  $\alpha = 0$ , bulk-to-shear-viscosity ratio  $R = 5$ , and power-law exponent  $n = 4$  at time  $t = 0.5$  corresponding to a local strain of 0.25 at the center of the inclusion. The pressure shadows around the inclusion are shown as porosity contours of 0.045 in blue and 0.055 in red. (b) Slice through the porosity field at  $x = \frac{1}{2}$ , for the same simulation at  $t = 0.5$ . (c) Second invariant of the strain-rate field at  $t = 0$ . (d) Radial integrals over porosity, for the same simulation at various times. (e) Simulations with  $\alpha = 0$  and  $R = 5$  at time  $t = 0.4$ , for various values of  $n$ .

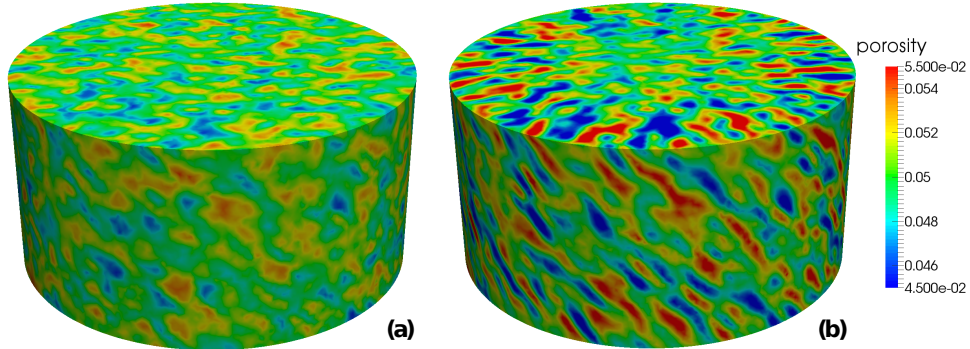


Figure 5: Example of a simulation with a random initial porosity field, with  $\alpha = 28$  and  $R = 1.7$ . (a) Initial porosity field. (b) Porosity field at  $t = 0.25$ .

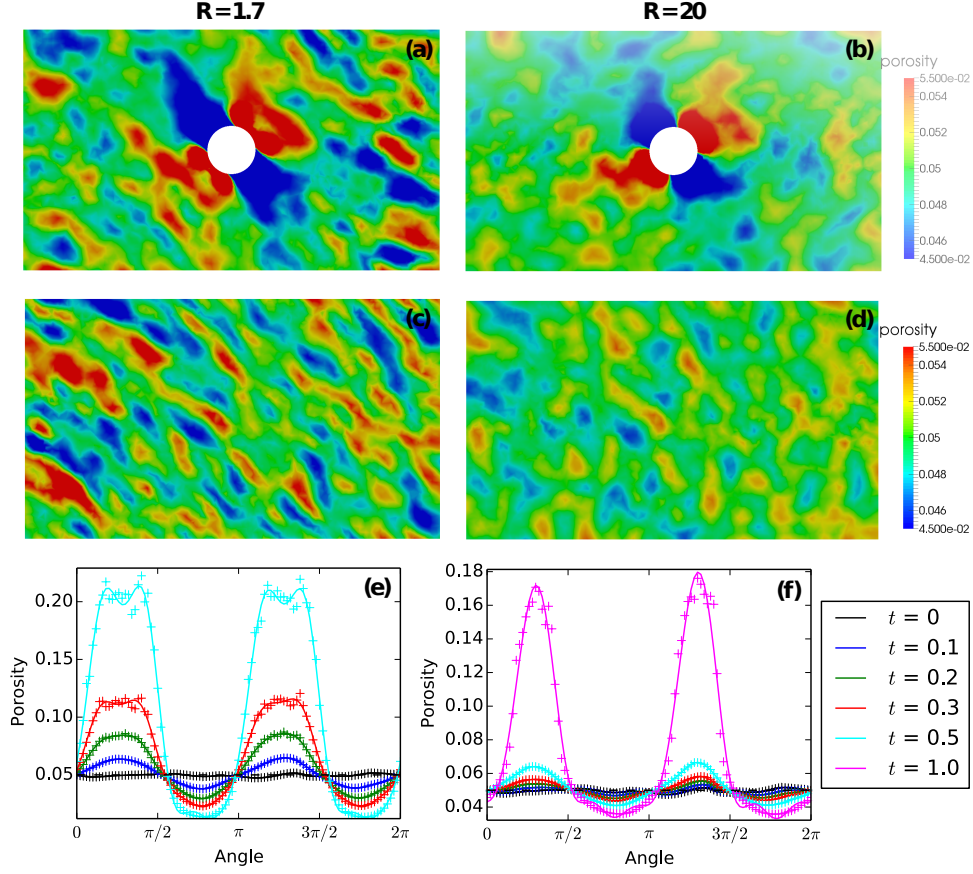


Figure 6: Results for simulations with a random initial porosity field and Newtonian viscosity. The local strain at the center of the inclusion corresponds to one half of the reported model time. **(a)** Slice through the porosity field on the inclusion side of the cylinder at  $x = 1/2$ , for a simulation with  $\alpha = 28$ ,  $R = 1.7$ , at  $t = 0.25$ . **(b)** Slice through porosity field on the inclusion side of the cylinder, for a simulation with  $\alpha = 28$ ,  $R = 20$ , at  $t = 1.0$ . **(c)** Slice through the porosity field on the side of the cylinder opposite the inclusion at  $x = -\frac{1}{2}$ , with  $\alpha = 28$ ,  $R = 1.7$ , at  $t = 0.25$ . **(d)** Slice through the porosity field on the side of the cylinder opposite the inclusion, with  $\alpha = 28$ ,  $R = 20$ , at  $t = 1.0$ . **(e)** Radial integrals over porosity, for the simulation with  $\alpha = 28$ ,  $R = 1.7$ , at various times  $t$ . The solid lines are fits with Fourier functions with the lowest nine coefficients included. **(f)** Radial integrals over porosity, for the simulation with  $\alpha = 28$ ,  $R = 20$ , at various times  $t$ .

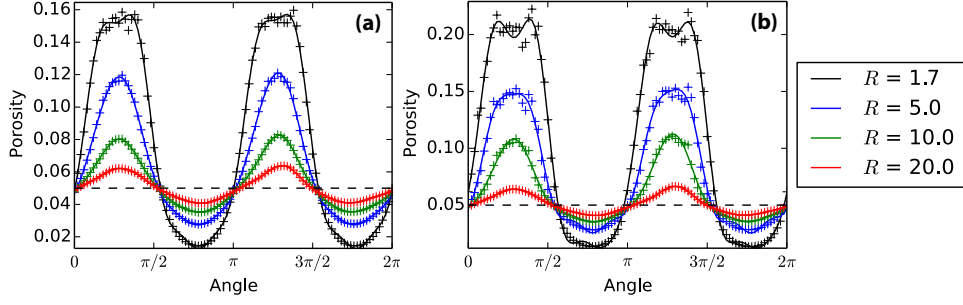


Figure 7: Radial integrals over porosity for simulations with a random initial porosity field and Newtonian viscosity, with various values of bulk-to-shear-viscosity ratio  $R$ . The solid lines are fits with Fourier functions with the lowest nine coefficients included. **(a)** Simulations with  $\alpha = 15$  at  $t = 0.5$ , for various values of  $R$ . **(b)** Simulations with  $\alpha = 28$  at  $t = 0.5$ , for various values of  $R$ .

in the  $R = 1.7$  case than in the  $R = 20$  case. In the latter case, the porosity shadows even display an advected pattern at large strains (represented by sharp peaks much like the simulation with a uniform initial porosity field in Figure 2c), indicating that the growth of porosity is less dominant than its advection for such large  $R$ .

Melt-rich bands only develop in simulations with sufficiently large  $\alpha$  and small  $R$ , as illustrated by the more pronounced widening and flattening of high-porosity peaks in the integrals in Figure 7. This is in line with the expected growth rates of melt-rich bands derived using linear stability analysis and presented in Appendix B.2. The linear stability analysis predicts melt bands to grow initially exponentially ( $\propto \exp(\dot{\epsilon}t)$ ) at a dimensionless rate

$$\dot{s} = \frac{\alpha(1 - \phi_0)}{R + \frac{4}{3}}, \quad (17)$$

which indicates that melt-rich bands are expected to grow faster for larger  $\alpha$  and smaller  $R$ .

### 3.3 Model regimes

Figure 8 summarizes the results of our parameter study of porosity exponent  $\alpha$  and bulk-to-shear-viscosity ratio  $R$  for simulations with a random initial porosity field and Newtonian rheology. The overall pattern is similar to that found in the two-dimensional study of *Alisic et al.* (2014): melt-rich bands only develop for  $R \leq 5$  and large  $\alpha$ . The region of the parameter space in which bands develop is slightly larger for the three-dimensional geometry compared to a two-dimensional case (see *Alisic et al.* (2014, Figure 10)), and the maximum strain achieved in the simulations is significantly larger. This might be explained by the fact that the amplitudes of pressure shadows decay faster away from the inclusion in three dimensions compared to two dimensions (as  $r^{-3}$  rather than  $r^{-2}$ , *Rudge* (2014)), resulting in less dominant pressure shadows compared to other features developing in the porosity field.

## 4 Discussion

The simulations in this study display several of the main features observed in the laboratory experiments by *Qi et al.* (2013), such as the pressure shadows around the spherical inclusion. For small bulk-to-shear-viscosity ratios, melt-rich bands develop throughout the medium, including in the vicinity of the inclusion. However, these bands do not have the dominance observed in the laboratory experiments, where they grow as very straight and pervasive features directly adjacent to the inclusion, overprinting the pressure shadows around the inclusion. In contrast,



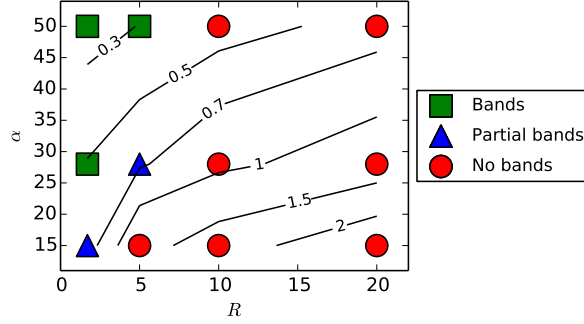


Figure 8: Summary of parameter study of bulk-to-shear-viscosity ratio  $R$  versus porosity exponent  $\alpha$ . Red circles indicate that no significant development of melt-rich bands takes place during a simulation with the specified combination of  $R$  and  $\alpha$ ; green squares indicate the presence of melt-rich bands. Blue triangles indicate development of melt-rich bands only away from the inclusion. The black contours denote the maximum strain achieved at the outer edge of the cylinder before the porosity goes out of bounds and the simulations end ( $\phi < 0$  or  $\phi > 1$ ).

the bands found in the numerical simulations grow to shorter lengths and do not overprint the porosity structure around the inclusion. Furthermore, simulations with and without random initial porosity perturbations using a given combination of  $\alpha$  and  $R$  and a Newtonian rheology run to the same maximum model strain before going out of bounds. This behavior, along with the fact that melt bands form for a larger  $(\alpha, R)$  parameter space away from the inclusion than near it, are indications that in our models the pressure shadows around the inclusion are dominant over any bands that form in simulations with random heterogeneities. Several recent studies investigate alternative constitutive relations (*Takei and Katz, 2013; Katz and Takei, 2013; Rudge and Bercovici, 2015*) that could potentially affect the balance of pressure shadows and melt-rich band formation near the inclusion.

The dominance of pressure shadows also points to a key deficiency in current models of two-phase-flow: the models contain no physics that sufficiently limit porosity growth, which results in the porosity field in our models growing until reaching unity, at which time the simulations are terminated. Realistically, the governing equations are only valid for porosities much smaller than unity. A second consequence of the porosity weakening rheology in our model is the lack of a minimum length scale (width) to which melt-rich bands will evolve. This means that the thickness of bands in simulations is ultimately dictated by the grid spacing, and therefore the solutions are resolution dependent.

It should be noted that our numerical simulations have a different velocity boundary condition on the sides of the cylinder than the experiments by *Qi et al. (2013)*. In those experiments, velocity is only prescribed on the top and bottom of the cylinder, and the side boundary can slip freely. In contrast, in our simulations the velocity is fully prescribed on all outside boundaries, leading to a potentially more constrained model.

In simulations with a rheology that is also strain-rate-dependent, limitations on numerical resolution near the inclusion prevented evolution to high strains. Therefore the regime where amplitudes of porosity variations were large enough to allow the porosity-weakening to become dominant over strain-rate effects was typically not reached, and bands would not develop within the simulation time.

In future numerical studies, it would be helpful to utilize a significantly higher resolution near the inclusion in such simulations, so that the strain-rate gradients can be better resolved. In addition, much could be gained from obtaining higher-resolution images of pressure shadows in experiments: the details of the shape of the shadows could help with identification of the prevailing deformation mechanism (diffusion creep or dislocation creep with large power-law



exponent  $n$ ).

## 5 Conclusions

We have modeled the behavior of partially molten material with an inclusion under torsion using three-dimensional numerical solutions to the equations of two-phase flow. Recent laboratory experiments with a similar setup display a competition between pressure shadows forming around the inclusion and melt-rich bands that develop throughout the partially molten medium. In our numerical simulations, the pressure shadows around the inclusion are reproduced for all tested combinations of bulk-to-shear-viscosity ratio and porosity exponent of the shear viscosity. In contrast, melt-rich bands only develop for small bulk-to-shear-viscosity ratios of five or less. We conclude that it is more difficult to form melt-rich bands near the inclusion, which provides a strong perturbation to the pressure field in the form of pressure shadows. Comparing this study with our earlier work in two dimensions, we show that the pressure shadows are less dominant in three dimensions, resulting in more pervasive development of melt-rich bands. For strain-rate dependent viscosity, the shape of the pressure shadows is significantly different compared to Newtonian cases. This variation in shape could be utilized to pinpoint the dominant deformation mechanism around the inclusion in future experiments.

## A Pressure splitting and nondimensionalization of the governing equations

The dimensional equations for two-phase flow are:

$$\frac{\partial \phi}{\partial t} - \nabla \cdot (1 - \phi) \mathbf{u}_s = 0, \quad (18)$$

$$\nabla \cdot \bar{\mathbf{u}} = 0, \quad (19)$$

$$\phi(\mathbf{u}_f - \mathbf{u}_s) = -\frac{K_\phi}{\mu_f} \nabla p_f, \quad (20)$$

$$\nabla \cdot \bar{\boldsymbol{\sigma}} = \mathbf{0}, \quad (21)$$

where  $\phi$  denotes porosity,  $t$  time, and  $\mathbf{u}_s$  and  $\mathbf{u}_f$  the solid and fluid velocities, respectively. Bulk properties are denoted with an overbar, where a bulk quantity  $\bar{a} = \phi a_f + (1 - \phi) a_s$ . Furthermore,  $K_\phi$  is the permeability,  $\mu_f$  the fluid viscosity,  $p_f$  the fluid pressure, and  $\bar{\boldsymbol{\sigma}}$  is the bulk stress tensor.

We define the bulk stress tensor in terms of the fluid pressure  $p_f$ , compaction pressure  $p_c$ , and the deviatoric stress tensor  $\bar{\boldsymbol{\tau}}$ :

$$\bar{\boldsymbol{\sigma}} = -p_f \mathbf{I} - p_c \mathbf{I} + \bar{\boldsymbol{\tau}}, \quad (22)$$

$$p_c = -\zeta \nabla \cdot \mathbf{u}_s, \quad (23)$$

$$\bar{\boldsymbol{\tau}} = 2\eta \dot{\boldsymbol{\epsilon}} = \eta \left( \nabla \mathbf{u}_s + (\nabla \mathbf{u}_s)^T - \frac{2}{3} (\nabla \cdot \mathbf{u}_s) \mathbf{I} \right), \quad (24)$$

where  $\mathbf{I}$  is the identity tensor,  $\zeta$  the bulk viscosity,  $\eta$  the shear viscosity, and  $\dot{\boldsymbol{\epsilon}}$  the deviatoric strain rate tensor.

We can now write a new system of equations using  $\mathbf{u}_s$ ,  $p_f$ ,  $p_c$ , and  $\phi$  as unknowns:

$$\frac{\partial \phi}{\partial t} - \nabla \cdot (1 - \phi) \mathbf{u}_s = 0, \quad (25)$$

$$-\nabla \cdot \mathbf{u}_s + \nabla \cdot \left( \frac{K_\phi}{\mu_f} \nabla p_f \right) = 0, \quad (26)$$

$$-\nabla \cdot \mathbf{u}_s - \zeta^{-1} p_c = 0, \quad (27)$$

$$-\nabla \cdot \bar{\boldsymbol{\tau}} + \nabla p_f + \nabla p_c = \mathbf{0}. \quad (28)$$

Constitutive properties are defined in this study as follows:

$$K_\phi = K_{\text{ref}} \left( \frac{\phi}{\phi_0} \right)^n, \quad (29)$$

$$\eta = \eta_{\text{ref}} \left( \frac{\dot{\epsilon}}{\dot{\epsilon}_{\text{ref}}} \right)^{-q} e^{-\alpha(\phi - \phi_0)}, \quad (30)$$

$$\zeta = \zeta_{\text{ref}} \left( \frac{\dot{\epsilon}}{\dot{\epsilon}_{\text{ref}}} \right)^{-q} e^{-\alpha(\phi - \phi_0)} \left( \frac{\phi}{\phi_0} \right)^{-m} = R\eta \left( \frac{\phi}{\phi_0} \right)^{-m}, \quad (31)$$

where  $n = 2$ ,  $m = 1$ , and  $\alpha$  is the porosity exponent and  $K_{\text{ref}}$  denotes the permeability at the reference porosity  $\phi_0$ . The second invariant of the deviatoric strain-rate tensor  $\dot{\epsilon}$  is given by:

$$\dot{\epsilon} = \left( \frac{1}{2} \dot{\epsilon} : \dot{\epsilon} \right)^{1/2}, \quad (32)$$

and  $q$  is related to the power law exponent  $\mathbf{n}$  by

$$q = 1 - \frac{1}{\mathbf{n}}. \quad (33)$$

The reference value of the second invariant is chosen as

$$\dot{\epsilon}_{\text{ref}} = \frac{\dot{\gamma}\rho}{2H}. \quad (34)$$

which is the value the second invariant takes on the curved boundary of the cylinder under the imposed torsion field.  $H$  is the radius of the cylinder and  $\dot{\gamma}$  is the imposed shear strain rate on the curved boundary.  $\eta_{\text{ref}}$  and  $\zeta_{\text{ref}}$  thus represent the shear and bulk viscosities at the curved boundary when the porosity is uniform and equal to  $\phi_0$ . The bulk-to-shear-viscosity ratio  $R$  is given by  $\zeta_{\text{ref}}/\eta_{\text{ref}}$ .

To complete the problem, boundary conditions are applied as follows:

$$-\frac{K_\phi}{\mu_f} \nabla p_f \cdot \mathbf{n} = 0 \text{ on } \partial\Omega, \quad (35)$$

$$\mathbf{u}_s = \mathbf{w} \text{ on } \partial\Omega, \quad (36)$$

where  $\mathbf{w}$  is a prescribed solid velocity, and the boundaries are taken to be impermeable.

We must now define a convention for nondimensionalizing the governing equations, using primes for dimensionless quantities:

$$\begin{aligned} \mathbf{x} &= H\mathbf{x}', & \mathbf{u}_s &= H\dot{\gamma}\mathbf{u}_s', & t &= \dot{\gamma}^{-1}t', \\ p_f &= \eta_{\text{ref}}\dot{\gamma}p_f', & p_c &= \eta_{\text{ref}}\dot{\gamma}p_c', \\ K_\phi &= K_{\text{ref}}K_\phi', & \eta &= \eta_{\text{ref}}\eta', & \zeta &= \zeta_{\text{ref}}\zeta'. \end{aligned} \quad (37)$$

The dimensionless system of equations then becomes, after dropping the primes, equations (1)–(4) in the main text.

## B Analysis and code benchmarks

### B.1 Instantaneous compaction around an inclusion

The instantaneous rate of compaction around a spherical inclusion in an unbounded medium with uniform porosity can be derived analytically (*McKenzie and Holness, 2000; Rudge, 2014*), which therefore lends itself for benchmarking our numerical method.

In *Rudge* (2014) analytical solutions were presented for compacting flow past a sphere in far-field simple shear. Here we generalize this solution to the case of a far-field torsional flow. We follow the approach of *Rudge* (2014) in this appendix, which has a different set of coordinates to the main body of this paper, with the center of the sphere being the origin of the coordinate system. In Cartesian coordinates the far-field torsional flow takes the form

$$\mathbf{u}_s^\infty = \dot{I} \left( -(y - y_0)(z - z_0), (x - x_0)(z - z_0), 0 \right), \quad (38)$$

where the origin of the torsional flow is at  $(x_0, y_0, z_0)$  and  $\dot{I}$  is the twist rate. The above can be decomposed into irreducible Cartesian tensors as

$$\mathbf{u}_s^\infty = \mathbf{V} + \boldsymbol{\Omega} \times \mathbf{x} + \mathbf{E} \cdot \mathbf{x} - \frac{1}{3} \mathbf{x} \times (\boldsymbol{\theta} \cdot \mathbf{x}), \quad (39)$$

where

$$\mathbf{V} = \dot{I} (-y_0 z_0, x_0 z_0, 0), \quad (40)$$

$$\boldsymbol{\Omega} = \dot{I} \left( \frac{x_0}{2}, \frac{y_0}{2}, -z_0 \right), \quad (41)$$

$$\mathbf{E} = \dot{I} \begin{pmatrix} 0 & 0 & y_0/2 \\ 0 & 0 & -x_0/2 \\ y_0/2 & -x_0/2 & 0 \end{pmatrix}, \quad (42)$$

$$\boldsymbol{\theta} = \dot{I} \begin{pmatrix} -1 & 0 & 0 \\ 0 & -1 & 0 \\ 0 & 0 & 2 \end{pmatrix}, \quad (43)$$

and  $\mathbf{x} = (x, y, z)$  is the position vector. According to the Faxén laws a sphere placed at the origin in such a flow will translate with velocity  $\mathbf{V}$  and rotate with angular velocity  $\boldsymbol{\Omega}$ , provided that there is no net force or torque on the sphere. The compacting flow past the sphere can be calculated as a linear superposition of the flow due to pure strain  $\mathbf{E} \cdot \mathbf{x}$  (*Rudge*, 2014, Section 5) and that due to the vortlet flow  $-\frac{1}{3} \mathbf{x} \times (\boldsymbol{\theta} \cdot \mathbf{x})$  (a quadratic flow, not considered in *Rudge* (2014)). The vortlet flow is characterized by the second-rank pseudo-tensor  $\boldsymbol{\theta}$  which is equal to the vorticity gradient. The perturbation flow satisfies boundary conditions

$$\tilde{\mathbf{u}}_s|_{r=a} = \frac{1}{3} \mathbf{x} \times (\boldsymbol{\theta} \cdot \mathbf{x}), \quad \nabla \tilde{p}_f \cdot \mathbf{n}|_{r=a} = 0, \quad (44)$$

$$\tilde{\mathbf{u}}_s \rightarrow \mathbf{0}, \quad \tilde{p}_f \rightarrow 0, \quad \text{as } r \rightarrow \infty, \quad (45)$$

where  $r = |\mathbf{x}|$  is distance from the center of the sphere, and  $a$  is the radius of the sphere. The solution to the governing equations with these boundary conditions does not involve compaction and is simply a Stokes flow, given by

$$\tilde{\mathbf{u}}_s = \frac{a^5}{3r^5} \mathbf{x} \times (\boldsymbol{\theta} \cdot \mathbf{x}), \quad (46)$$

$$\tilde{p}_f = 0. \quad (47)$$

Since the quadratic flow does not involve compaction, the instantaneous compaction rate for a sphere in a torsional field is the same as that for pure and simple shear, given by *Rudge* (2014, eqns. (5.51) and (5.63)). When the compaction length is large compared to the domain size, the behavior can be well described by the large-compaction-length asymptotic limit of the equations, where the instantaneous compaction rate and fluid pressure are given by

$$\nabla \cdot \mathbf{u}_s = \frac{15\nu}{2\nu + 3} \left( \frac{a}{r} \right)^3 \frac{\mathbf{x} \cdot \mathbf{E} \cdot \mathbf{x}}{r^2}, \quad (48)$$

$$p_f = \frac{\mu_f a^2}{K_{\text{ref}}} \frac{5\nu}{6(2\nu + 3)} \left[ \left( \frac{a}{r} \right)^3 - \frac{3a}{r} \right] \frac{\mathbf{x} \cdot \mathbf{E} \cdot \mathbf{x}}{r^2}, \quad (49)$$

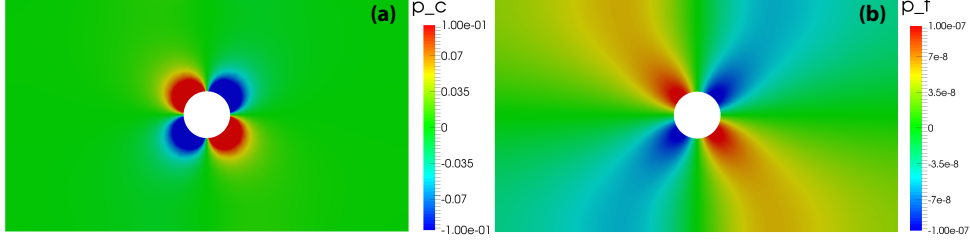


Figure 9: Instantaneous pressure fields for a simulation with inclusion size 0.1, porosity exponent  $\alpha = 28$ , bulk-to-shear-viscosity ratio  $R = 5/3$ , and stress exponent  $n = 1$ . (a) Compaction pressure. (b) Fluid pressure.

where  $\nu \equiv \eta_{\text{ref}} / (\zeta_{\text{ref}} + 4\eta_{\text{ref}}/3) = (R + 4/3)^{-1}$ . The above solution is identical to that given in equations (30) and (32) of *McKenzie and Holness* (2000).

In Figure 9 we show the numerically-calculated instantaneous compaction pressure and fluid pressure on the two-dimensional slice indicated in Figure 1b, resulting from the imposed torsion. We use a large compaction length with  $D = 100$ , and the same cylindrical mesh as outlined in Section 2.3. The numerically-calculated compaction pressure, shown in Figure 9a, very closely matches the analytical expression in (48). The fluid pressure, shown in Figure 9b, matches less well, with the expected quadrupole pattern of (49) disturbed at the top and bottom boundaries of the finite computational domain. That the fluid pressure is affected more by the boundaries than the compaction pressure is to be expected from the analytical expressions in (48) and (49); compaction pressure decays rapidly away from the inclusion, as  $r^{-3}$ , whereas fluid pressure decays much more slowly, as  $r^{-1}$ , and thus the fluid pressure feels effects at larger distances.

For further validation of the numerical simulations, we compute  $L_2$  error norms for the fluid pressure  $p_f$ , compaction pressure  $p_c$ , and solid velocity  $\mathbf{u}_s$ , with respect to the analytical solutions. We define the following error for a field  $\chi$ :

$$e_{L_2} = \frac{\|\chi^N - \chi^A\|_2}{\|\chi^A\|}, \quad (50)$$

where the numerical field is denoted by  $\chi^N$  and the analytical solution by  $\chi^A$ . We compute this for a series of inclusion radii between 0.05 and 0.2, as shown in Figure 10. The  $L_2$  error decreases with decreasing inclusion radius. This indicates that the error with respect to the analytical solution results from the presence of boundaries in the numerical domain, which do not exist in the analytical solution. This effect becomes less dominant when the inclusion is further away from the outside cylinder boundaries, i.e., for smaller inclusions. In addition, the  $L_2$  error is larger for the fluid pressure than for the compaction pressure. This is due to the same boundary effects as observed in Figure 9.

## B.2 Linear stability analysis of melt bands under torsion

Linear stability analysis provides important insight into the expected growth rate of melt bands (e.g. *Stevenson*, 1989; *Spiegelman*, 2003; *Katz et al.*, 2006; *Butler*, 2009; *Takei and Katz*, 2013; *Rudge and Bercovici*, 2015). The solutions arising from linear stability analysis can also be used as a check on numerical solutions of the full set of governing equations (see *Alisic et al.* (2014, Appendix C2)). In this appendix we present a linear stability analysis of melt bands under torsion in an infinite cylinder for our chosen rheology, and use the solutions to benchmark our numerical code. The analysis closely follows an earlier linear stability analysis of melt bands under torsion by *Takei and Katz* (2013). In *Takei and Katz* (2013) it was assumed that perturbation wavenumbers are large, which allows the neglect of various radial derivatives in the analysis. We do not make this assumption here, and instead solve numerically for the radial variation.

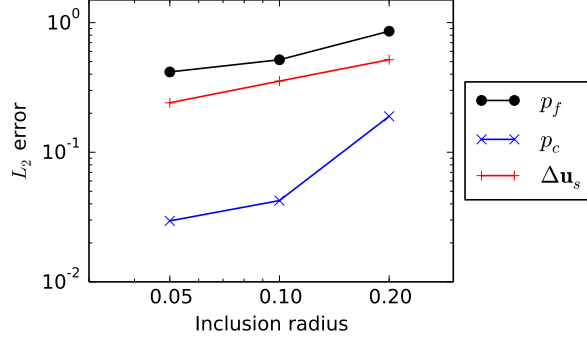


Figure 10:  $L_2$  error norms computed for simulations with different inclusion radii, for fluid pressure  $p_f$ , compaction pressure  $p_c$ , and solid velocity perturbation  $\Delta \mathbf{u}_s$  with respect to a torsional velocity field without an inclusion.

The base state solution has a uniform porosity  $\phi_0$  and solid velocity  $\mathbf{u}_0$  given in cylindrical coordinates  $(\rho, \psi, z)$  as

$$\mathbf{u}_0 = \dot{I} \rho z \hat{\psi}, \quad (51)$$

where  $\dot{I}$  is the twist rate. The twist rate  $\dot{I}$  is related to the shear strain rate  $\dot{\gamma}$  on the cylinder edge by  $\dot{\gamma} = \dot{I}H$ . The base state solution has zero pressure everywhere ( $p_0 = 0$ ), is not compacting such that  $\mathcal{C}_0 \equiv \nabla \cdot \mathbf{u}_0 = 0$ , and has a strain-rate-tensor with only the  $(\psi, z)$  component non-zero,

$$\dot{\mathbf{e}}_0 = \dot{I} \frac{\rho}{2} (\hat{\psi} \hat{z} + \hat{z} \hat{\psi}). \quad (52)$$

We seek small perturbations about this base state of the form

$$\phi = \phi_0 + \epsilon \phi_1 + \dots, \quad (53)$$

$$\mathbf{u}_s = \mathbf{u}_0 + \epsilon \mathbf{u}_1 + \dots, \quad (54)$$

$$p_f = 0 + \epsilon p_1 + \dots. \quad (55)$$

Substituting (53)–(55) into the governing equations (18)–(21) leads to equations at first order in  $\epsilon$  given by

$$\frac{D_0 \phi_1}{Dt} = (1 - \phi_0) \mathcal{C}_1, \quad (56)$$

$$\mathcal{C}_1 - \frac{K_0}{\mu_f} \nabla^2 p_1 = 0, \quad (57)$$

$$\nabla \cdot \bar{\boldsymbol{\sigma}}_1 = 0, \quad (58)$$

$$\bar{\boldsymbol{\sigma}}_1 = -p_1 \mathbf{I} + \zeta_0 \mathcal{C}_1 \mathbf{I} + 2\eta_0 \dot{\mathbf{e}}_1 + 2\eta_1 \dot{\mathbf{e}}_0, \quad (59)$$

where  $\frac{D_0}{Dt} \equiv \frac{\partial}{\partial t} + \mathbf{u}_0 \cdot \nabla$ .

When the rheology is non-Newtonian, the base state viscosities vary with radius according to

$$\eta_0 = \eta_{\text{ref}} (\rho/H)^{-q}, \quad (60)$$

$$\zeta_0 = \zeta_{\text{ref}} (\rho/H)^{-q}. \quad (61)$$

Expanding the rheological law (30) to first order in  $\epsilon$  yields

$$\eta_1 = \eta_0 \left( -\alpha \phi_1 - q \frac{\dot{\mathbf{e}}_1 : \dot{\mathbf{e}}_0}{2\dot{\mathbf{e}}_0^2} \right) = \eta_0 \left( -\alpha \phi_1 - q \frac{\dot{e}_{1\psi z}}{\dot{\mathbf{e}}_0} \right). \quad (62)$$

The expected growth rate of bands can be determined by replacing (56) by

$$\dot{s}\phi_1 = (1 - \phi_0)\mathcal{C}_1, \quad (63)$$

and solving the eigenvalue problem described by (57)–(59) and (62)–(63) for the instantaneous growth rate  $\dot{s}$ . The finite element method can be used to numerically solve for the eigenfunctions and eigenvalues of the linear stability equations. Equations (57)–(59) and (62)–(63) can be cast into a weak form for trial functions  $(\mathbf{u}, p)$  and test functions  $(\mathbf{v}, q)$  as

$$\int_V 2\eta_0 \dot{\mathbf{e}}^u : \dot{\mathbf{e}}^v + \zeta_0 \mathcal{C}^u \mathcal{C}^v - p \mathcal{C}^v - q \mathcal{C}^u - \frac{K_0}{\mu_f} \nabla p \cdot \nabla q - 4\eta_0 q \dot{e}_{\psi z}^u \dot{e}_{\psi z}^v dV = \lambda \int_V 4\eta_0 \dot{\mathbf{e}}_0 \mathcal{C}^u \dot{e}_{\psi z}^v dV, \quad (64)$$

$$\dot{\mathbf{e}}^u \equiv \frac{1}{2} \left( \nabla \mathbf{u} + (\nabla \mathbf{u})^T \right) - \frac{1}{3} (\nabla \cdot \mathbf{u}) \mathbf{I}, \quad (65)$$

$$\mathcal{C}^u = \nabla \cdot \mathbf{u}, \quad (66)$$

where the subscripts 1 referring to the first order state have been neglected for clarity. The eigenvalue  $\lambda$  is related to the growth rate  $\dot{s}$  by

$$\lambda = \frac{\alpha(1 - \phi_0)}{\dot{s}}. \quad (67)$$

The impermeable and no-slip boundary conditions (35) and (36) on the cylinder edge lead to the vanishing of surface integral terms in the weak form (64).

The three-dimensional weak form (64) can be reduced to a weak form for the radial coordinate alone using symmetry considerations. Invariance of the cylinder under rotation about its axis, and invariance under translation in the  $z$  direction, suggests looking for eigenfunctions proportional to  $e^{in\psi + ihz}$  where  $n$  is the angular wavenumber, and  $h$  is the vertical wavenumber. Substituting solutions of this form

$$u_\rho = U_\rho(\rho) e^{in\psi + ihz}, \quad (68)$$

$$u_\psi = iU_\psi(\rho) e^{in\psi + ihz}, \quad (69)$$

$$u_z = iU_z(\rho) e^{in\psi + ihz}, \quad (70)$$

$$p = P(\rho) e^{in\psi + ihz}, \quad (71)$$

and corresponding complex conjugates for test functions into (64) leads to purely radial integrals where  $dV \rightarrow 2\pi\rho d\rho$ . The integrands are real, and the resulting radial eigenfunction problem was solved using FEniCS/DOLFIN (*Logg and Wells, 2010*) and the eigenvalue solver SLEPc (*Hernandez et al., 2005*). An example eigenfunction calculated using this approach is shown in Figure 11.

### B.2.1 A special case: Newtonian melt bands under torsion in an infinite domain

There is a special case of the linear stability analysis for which a complete analytical solution can be obtained. This is the case when the rheology is Newtonian ( $n = 1$ ), and the domain of interest is infinite. In this case the solenoidal component of the flow is decoupled from the irrotational component, simplifying the analysis (*Spiegelman, 1993, 2003*). The linear stability equations are

$$\frac{\partial \phi_1}{\partial t} + \dot{\Gamma} z \frac{\partial \phi_1}{\partial \psi} = (1 - \phi_0)\mathcal{C}_1, \quad (72)$$

$$-\nabla^2 \mathcal{C}_1 + \delta^{-2} \mathcal{C}_1 = -2\nu\alpha \dot{\Gamma} \frac{\partial^2 \phi_1}{\partial z \partial \psi}, \quad (73)$$

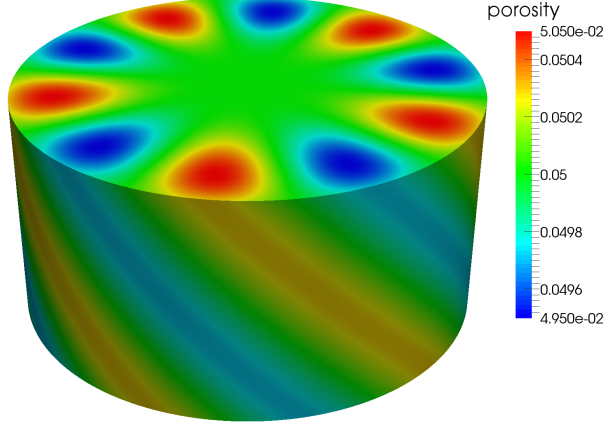


Figure 11: Porosity field for a particular eigenfunction of the linear stability equations. This eigenfunction has angular wavenumber  $n = 5$ , and vertical wavenumber  $h$  chosen such that the angle of the bands to the shear plane is  $45^\circ$  on the edge of the cylinder. The bulk-to-shear-viscosity ratio  $R = 5/3$  and the power law exponent  $\mathbf{n} = 1$ . The compaction length is large (100 times the cylinder radius). The eigenfunction shown is the fastest growing mode with this choice of  $n$  and  $h$ .

where (72) follows from (56), and (73) is a result of combining the divergence of (58) with (57), (59), and (62),  $\delta$  is the compaction length (5), and  $\nu = \eta_{\text{ref}} / (\zeta_{\text{ref}} + 4\eta_{\text{ref}}/3)$ . Solutions to (72) and (73) can be found in the form of cylindrical harmonics (eigenfunctions of the Laplacian operator in cylindricals),

$$\phi_1 = \Phi(t)J_n(\lambda\rho)e^{in\psi+ih(t)z}, \quad (74)$$

$$\mathcal{C}_1 = C(t)J_n(\lambda\rho)e^{in\psi+ih(t)z}, \quad (75)$$

where  $J_n(z)$  is a Bessel function of the first kind and  $h(t)$  is the vertical wavenumber, which varies with time as

$$h(t) = h_0 - \dot{\Gamma}nt, \quad (76)$$

due to the advection. Note that

$$\nabla^2 \mathcal{C}_1 = -k^2(t)\mathcal{C}_1, \quad (77)$$

$$k^2(t) = \lambda^2 + h^2(t). \quad (78)$$

Substituting (74) and (75) into (72) and (73) yields

$$\dot{\Phi}(t) = (1 - \phi_0)C(t), \quad (79)$$

$$\left(\delta^{-2} + k^2(t)\right)C(t) = 2\nu\alpha\dot{\Gamma}nh(t)\Phi(t), \quad (80)$$

which can be combined to give

$$\dot{\Phi}(t) = \frac{2\nu\alpha\dot{\Gamma}(1 - \phi_0)nh(t)}{\delta^{-2} + k^2(t)}\Phi(t), \quad (81)$$

and integrated to give

$$\Phi(t) = \left(\frac{\delta^{-2} + k^2(0)}{\delta^{-2} + k^2(t)}\right)^{\nu\alpha(1-\phi_0)}. \quad (82)$$

These expressions closely mirror the expressions for simple shear given by *Spiegelman* (2003): compare (81) and (82) here with equations (27) and (33), respectively, from *Spiegelman* (2003).

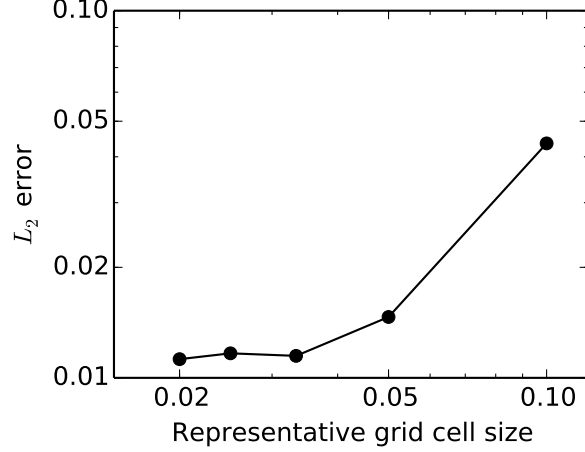


Figure 12:  $L_2$  error norms of growth rate at the center-plane of the cylinder, computed for numerical simulations with different resolutions. The eigenfunction tested is shown in Figure 11.

The expressions are identical, except with the appropriate switch of angular wavenumbers for planar wavenumbers, and the difference in nondimensionalization.

In a cylinder of finite radius, common choices of boundary conditions on the cylinder edge (including no-slip) lead to a coupling of the solenoidal component of the flow and the irrotational component, which complicates the analysis given above. Nevertheless, this special solution can be used as a check on the numerical approach to calculating the eigenfunctions described in the preceding section. The special solution (74) and (81) was recovered numerically for a choice of boundary conditions that decouples the solenoidal flow from the irrotational. This choice of boundary condition is impermeable, and almost, but not quite, free-slip: on the cylinder edge  $u_\rho = 0$ ,  $\bar{\sigma}_{\rho z} = 0$ ,  $\bar{\sigma}_{\rho\psi} = -2\nu u_\psi/\rho$ , and  $\partial p_f/\partial \rho = 0$ . These boundary conditions imply that  $\partial \mathcal{C}/\partial \rho = 0$  on the cylinder edge, and restrict the allowable values of  $\lambda$  to the roots of the derivative of the Bessel function. As is the case for simple shear, the fastest growing modes occur for infinite wavenumbers. The maximum growth rate occurs as  $n \rightarrow \infty$ ,  $h \sim n/H$  (i.e., bands at  $45^\circ$  to the shear plane on the cylinder edge) where  $\dot{s} \rightarrow \nu\alpha(1 - \phi_0)\dot{\Gamma}H$ .

### B.2.2 Linear stability benchmark

We test the application code by numerically computing the instantaneous growth rate of porosity for an initial porosity field given by the eigenfunction shown in Figure 11. The numerically computed growth rate can be compared with the expected growth rate of the eigenfunction determined from the eigenvalue.

Figure 12 shows an example of such a comparison, where an error norm for growth rate is plotted against resolution for various mesh resolutions from approximately 10 to 50 elements in the vertical direction, to study the effect of grid size on the accuracy of the numerical method. It is important to note that the eigenfunctions are determined for a cylinder of infinite extent, whereas the simulation domain is a cylinder of finite extent. To mitigate the resulting boundary effects, the two are compared only on a slice through the center-plane of the cylinder, at  $z = 1/2$ . The  $L_2$  error norm is calculated for the local instantaneous growth rate of porosity on the slice, using equation (50). Generally, the error in growth rate on the center-plane decreases with increasing resolution (i.e., with decreasing grid size), until a limit is reached at a grid size around 0.03. For finer grids the error does not decrease any further, which we attribute to the effect of the top and bottom boundaries on the growth of porosity. Computed growth rates are typically within a few per cent of the expected growth rates, which gives us confidence that the



application code is solving the compaction equations effectively.

## Acknowledgements

This work was supported by the UK Natural Environment Research Council under grants NE/I023929/1 and NE/I026995/1. Computations were performed on the ARCHER UK National Supercomputing Service (<http://www.archer.ac.uk>). We thank Chris Richardson for all his support with running the simulations on ARCHER. Katz thanks the Leverhulme Trust for support.

## References

- Alisic, L., J. F. Rudge, R. F. Katz, G. N. Wells, and S. Rhebergen (2014), Compaction around a rigid, circular inclusion in partially molten rock, *J. Geophys. Res. - Solid Earth*, *119*(7), 5903–5920.
- Balay, S., S. Abhyankar, M. F. Adams, J. Brown, P. Brune, K. Buschelman, L. Dalcin, V. Eijkhout, W. D. Gropp, D. Kaushik, M. G. Knepley, L. C. McInnes, K. Rupp, B. F. Smith, S. Zampini, and H. Zhang (2015a), PETSc Web page.
- Balay, S., S. Abhyankar, M. F. Adams, J. Brown, P. Brune, K. Buschelman, L. Dalcin, V. Eijkhout, W. D. Gropp, D. Kaushik, M. G. Knepley, L. C. McInnes, K. Rupp, B. F. Smith, S. Zampini, and H. Zhang (2015b), PETSc users manual, *Tech. Rep. ANL-95/11 - Revision 3.6*, Argonne National Laboratory.
- Bercovici, D., and Y. Ricard (2003), Energetics of a two-phase model of lithospheric damage, shear localization and plate-boundary formation, *Geophys. J. Int.*, *152*, 581–596.
- Butler, S. L. (2009), The effects of buoyancy on shear-induced melt bands in a compacting porous medium, *Phys. Earth Planet. In.*, *173*(1-2), 51–59, doi:10.1016/j.pepi.2008.10.022.
- Hernandez, V., J. E. Roman, and V. Vidal (2005), SLEPc: A scalable and flexible toolkit for the solution of eigenvalue problems, *ACM Trans. Math. Software*, *31*(3), 351–362.
- Holtzman, B. K., N. J. Groebner, M. E. Zimmerman, S. B. Ginsberg, and D. L. Kohlstedt (2003), Stress-driven melt segregation in partially molten rocks, *Geochem. Geophys. Geosys.*, *4*, doi:10.1029/2001GC000258.
- Katz, R. F., and Y. Takei (2013), Consequences of viscous anisotropy in a deforming, two-phase aggregate: Part 2. Numerical solutions of the full equations, *J. Fluid Mech.*, *734*, 456–485.
- Katz, R. F., M. Spiegelman, and B. Holtzman (2006), The dynamics of melt and shear localization in partially molten aggregates, *Nature*, *442*, 676–679.
- Katz, R. F., M. G. Knepley, B. Smith, M. Spiegelman, and E. T. Coon (2007), Numerical simulation of geodynamic processes with the portable extensible toolkit for scientific computation, *Phys. Earth Planet. In.*, *163*, 52–68.
- Kelemen, P. B., G. Hirth, N. Shimizu, M. Spiegelman, and H. J. B. Dick (1997), A review of melt migration processes in the adiabatically upwelling mantle beneath oceanic spreading ridges, *Phil. Trans. R. Soc. London A*, *355*(1723), 283–318.
- King, D. S. H., M. E. Zimmerman, and D. L. Kohlstedt (2010), Stress-driven melt segregation in partially molten olivine-rich rocks deformed in torsion, *J. Petrol.*, *51*, 21–42.

- Logg, A., and G. N. Wells (2010), DOLFIN: Automated finite element computing, *ACM Trans Math Software*, 37(2), 20:1–20:28.
- Logg, A., K.-A. Mardal, and G. N. Wells (Eds.) (2012), *Automated Solution of Differential Equations by the Finite Element Method, Lecture Notes in Computational Science and Engineering*, vol. 84, Springer.
- McKenzie, D. (1984), The generation and compaction of partially molten rock, *J. Petrol.*, 25, 713–765, doi:10.1093/petrology/25.3.713.
- McKenzie, D., and M. Holness (2000), Local deformation in compacting flows: Development of pressure shadows, *Earth and Planetary Science Letters*, 180, 169–184.
- Mei, S., W. Bai, T. Hiraga, and D. Kohlstedt (2002), Influence of melt on the creep behavior of olivinebasalt aggregates under hydrous conditions, *Earth and Planetary Science Letters*, 201(3), 491–507.
- Qi, C., Y.-H. Zhao, and D. L. Kohlstedt (2013), An experimental study of pressure shadows in partially molten rocks, *Earth Plan. Sci. Lett.*, 382, 77–84.
- Rhebergen, S., G. N. Wells, R. F. Katz, and A. J. Wathen (2014), Analysis of block-preconditioners for models of coupled magma/mantle dynamics, *SIAM J. Sci. Comput.*, 36, A1960–A1977.
- Rhebergen, S., G. N. Wells, A. J. Wathen, and R. F. Katz (2015), Three-field block-preconditioners for models of coupled magma/mantle dynamics, *SIAM J. Sci. Comput.*, to appear.
- Rudge, J. F. (2014), Analytical solutions of compacting flow past a sphere, *J. Fluid. Mech.*, 746, 466–497.
- Rudge, J. F., and D. Bercovici (2015), Melt-band instabilities with two-phase damage, *Geophysical Journal International*, 201, 640–651.
- Simpson, G., M. Spiegelman, and M. I. Weinstein (2010), A multiscale model of partial melts: 2. Numerical results, *Journal of Geophysical Research*, 115, doi:10.1029/2009JB006376.
- Spiegelman, M. (1993), Flow in deformable porous-media. part 1. Simple analysis, *J. Fluid Mech.*, 247.
- Spiegelman, M. (2003), Linear analysis of melt band formation by simple shear, *Geochemistry, Geophysics, Geosystems*, 4(9), 8615, doi:10.1029/2002GC000499.
- Stevenson, D. J. (1989), Spontaneous small-scale melt segregation in partial melts undergoing deformation, *Geophys. Res. Lett.*, 16, 1067–1070.
- Takei, Y., and B. K. Holtzman (2009), Viscous constitutive relations of solid-liquid composites in terms of grain boundary contiguity: 1. Grain boundary diffusion control model, *Journal of Geophysical Research*, 114, doi:10.1029/2008JB005850.
- Takei, Y., and R. F. Katz (2013), Consequences of viscous anisotropy in a deforming, two-phase aggregate: Part 1. Governing equations and linearised analysis, *J. Fluid Mech.*, 734, 424–455.
- Tenczer, V., K. Stüwe, and T. D. Barr (2001), Pressure anomalies around cylindrical objects in simple shear, *Journal of Structural Geology*, 23, 777–788.